

Integrated Circuits and Electrode Interfaces for Noninvasive Physiological Monitoring

Sohmyung Ha, *Student Member, IEEE*, Chul Kim, *Student Member, IEEE*, Yu M. Chi, *Member, IEEE*, Abraham Akinin, *Student Member, IEEE*, Christoph Maier, *Member, IEEE*, Akinori Ueno, *Member, IEEE*, and Gert Cauwenberghs*, *Fellow, IEEE*

Abstract—This paper presents an overview of the fundamentals and state of the-art in noninvasive physiological monitoring instrumentation with a focus on electrode and optrode interfaces to the body, and micropower-integrated circuit design for unobtrusive wearable applications. Since the electrode/optrode–body interface is a performance limiting factor in noninvasive monitoring systems, practical interface configurations are offered for biopotential acquisition, electrode–tissue impedance measurement, and optical biosignal sensing. A systematic approach to instrumentation amplifier (IA) design using CMOS transistors operating in weak inversion is shown to offer high energy and noise efficiency. Practical methodologies to obviate $1/f$ noise, counteract electrode offset drift, improve common-mode rejection ratio, and obtain subhertz high-pass cutoff are illustrated with a survey of the state-of-the-art IAs. Furthermore, fundamental principles and state-of-the-art technologies for electrode–tissue impedance measurement, photoplethysmography, functional near-infrared spectroscopy, and signal coding and quantization are reviewed, with additional guidelines for overall power management including wireless transmission. Examples are presented of practical dry-contact and noncontact cardiac, respiratory, muscle and brain monitoring systems, and their clinical applications.

Index Terms—Biological signal sensing, biomedical electronics, body–electrode interface, electrode contacts, electrode–tissue impedance, functional near-infrared spectroscopy, health monitoring, instrumentation amplifier (IA), optrode interface, photoplethysmography, sensor interface.

I. INTRODUCTION

NONINVASIVE physiological monitoring technology has advanced tremendously over the years making a substan-

Manuscript received December 5, 2013; revised February 11, 2014; accepted February 16, 2014. Date of publication February 26, 2014; date of current version April 17, 2014. This work was supported in part by the National Science Foundation M3C EFRI-1137279, in part by The Defense Advanced Research Projects Agency, in part by the Texas Instruments, in part by the NEDO of Japan. The work of S. Ha was supported by a Fulbright fellowship. *Asterisk indicates corresponding author.*

S. Ha, C. Kim, A. Akinin, and C. Maier are with the Department of Bioengineering and the Institute for Neural Computation, Jacobs School of Engineering, University of California, San Diego, La Jolla, CA 92093 USA (e-mail: soha@ucsd.edu; chk079@ucsd.edu; aakinin@ucsd.edu; christoph.maier@ieeeg.org).

Y. M. Chi is with Cognionics Inc., San Diego, CA 92121 USA (e-mail: mikechi2@gmail.com).

A. Ueno is with the Department of Electrical and Electronic Engineering, Tokyo Denki University, Adachi-ku, Tokyo 120-8551, Japan (e-mail: ueno@mail.dendai.ac.jp).

*G. Cauwenberghs is with the Department of Bioengineering and the Institute for Neural Computation, Jacobs School of Engineering, University of California, San Diego, La Jolla, CA 92093 USA (e-mail: gert@ucsd.edu).

Color versions of one or more of the figures in this paper are available online at <http://ieeexplore.ieee.org>.

Digital Object Identifier 10.1109/TBME.2014.2308552

tial impact on medical diagnostics and personal healthcare, from the early fundamental advances in noncontact and dry sensing technology [1]–[3] to most recent advances extending the range of physiological sensing using imaging and electrical sensing technology abundantly available in handheld devices and household appliances [4]–[7]. CMOS technologies and circuit techniques have facilitated the development and miniaturization of innovative physiological sensing devices, improving the performance, power and monetary costs while ensuring the validity of medical information through analog and digital signal processing methods. These IC developments have permitted reliable noninvasive measurement of vital parameters and have spawned a variety of new instruments for clinical treatment and diagnosis.

Innovations by semiconductor technologies enable ambulatory continuous-time monitoring of patients even at home. This ubiquitous monitoring supported by modern IC technology can enable personalized healthcare and preemptive medicine, which are emerging solutions to soaring healthcare costs induced by the current demographical trend of increasing aging population. The patient-supporting sensors and systems not only extend the capability and accuracy of modern diagnostics, but also improve the patient’s everyday life. In addition, miniaturized electronic systems for biosignal sensing can be tailored to many nonclinical applications such as sports and entertainment.

Fig. 1(b) shows the main functional components of a generic IC for noninvasive physiological monitoring, comprising analog front-end (AFE), analog signal processor (ASP), analog-to-digital converter (ADC), digital signal processor (DSP), radio frequency (RF) communications, and power management. This review surveys these components with a focus on the core functions of AFE, ASP, and ADC implemented in low-noise, low-power custom integrated circuits, and tailored to the signal conditions and range of the physiological variables of interest. Foremost, a solid and thorough understanding of the electrode–body interface is of primary importance for accurate and reliable noninvasive physiological sensing and signal acquisition. The following section reviews fundamentals of electrode–body and optrode–body interfaces for biopotential acquisition, impedance measurement, and optics-based sensing.

II. NONINVASIVE ELECTRODE INTERFACES TO THE BODY

A. Electrode Interfaces for Biopotential Sensing

The coupling of biopotential signals from the body into the front-end amplifier is accomplished through electrodes. At a fundamental level, the electrode interfaces ionic currents in the

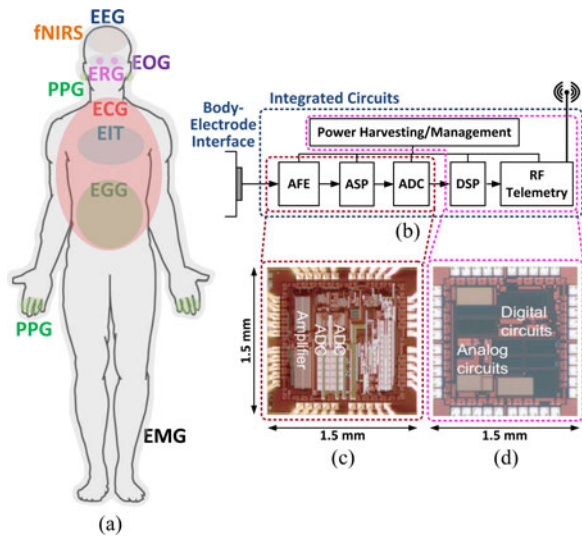


Fig. 1. Noninvasive physiological monitoring. (a) Signal modalities of electrical and vascular activity internal to the body available for measurement on the periphery. See Table I for glossary. (b) Integrated circuits (ICs) and electrode interfaces for signal acquisition, coding, and transmission. Example micrographs are shown for (c) a biopotential front-end and acquisition IC interfacing through bit-serial daisy chain with (d) a power and data telemetry IC [8].

TABLE I
NONINVASIVE PHYSIOLOGY AND BODY SIGNALS

Name	Carrier	Activity
EEG	Voltage	Brain rhythms
ECG	Voltage	Cardiac rhythms
EMG	Voltage	Muscle activation
EOG	Voltage	Eye movement
ERG	Voltage	Retinal potentials
EGG	Voltage	Stomach activity
EIT	Impedance	Lung activity
fNIRS	Optical	Neurovascular activity
PPG	Optical	Blood oxygenation

body with electrical currents in the electronic instrumentation. In practice, because the electrode comprises the first stage of the signal chain, its properties can dominate the overall noise and performance of the acquisition system making its design and selection crucially important.

Broadly speaking, there exist three classes of biopotential electrodes in the literature: wet, dry, and noncontact as shown in Fig. 2 [9], [13]. All types of electrodes ideally measure the exact same biopotential signals and are largely differentiated by the presence of a gel and the resulting contact impedance to the body.

Wet electrodes are the most common type and considered the “gold standard” for both clinical and research applications. A typical wet electrode consists of a silver–silver chloride (Ag/AgCl) metal that is surrounded by a wet or solid hydrogel, containing chloride. Other kinds of metals can be used (gold is common for EEG) if the dc stability of the Ag/AgCl electrode is not necessary. The primary drawbacks with wet electrodes are its longevity and comfort. Wet electrodes degrade as the moisture content evaporates limiting its useful lifetime to, at most, a

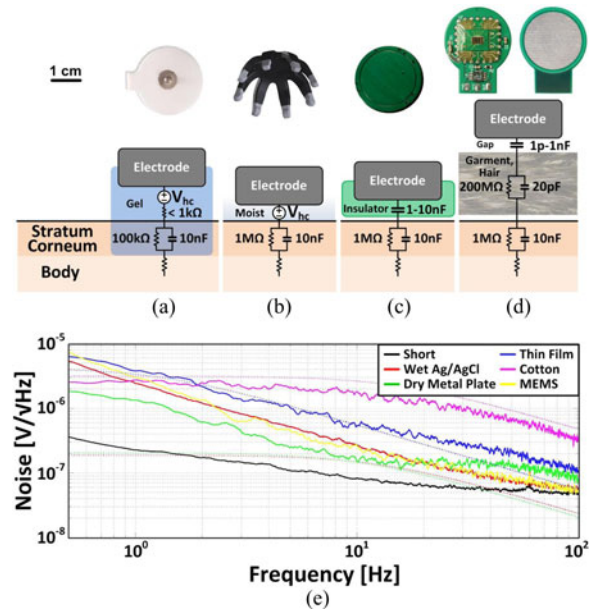


Fig. 2. Electrical coupling of the skin–electrode interface for various electrode topologies, including (a) wet-contact gel-based Ag/AgCl [9], (b) dry-contact flexible thru-hair sensor [10], (c) thin-film insulated capacitive metal plate [11], and (d) noncontact metal plate coupling through hair or clothing such as cotton [12]. (e) Measured noise spectrum of various electrode types, placed at close proximity on forearm at rest, along with predicted (dotted lines) thermal noise limits from measured skin–electrode coupling impedance data [9]. The instrumentation noise floor of the shorted amplifier is also shown for reference.

few days. Many users also report skin irritation and discomfort from the gels and adhesives that contact the skin.

Dry electrodes operate without the use of an explicit wet/gel coupling media. The metal in the electrode directly contacts the skin to couple biopotential signals. In practice, however, virtually all dry electrodes still rely on some degree of moisture which is gathered from the environment or emitted from the body (e.g., sweat). Compared with the wet electrodes, the performance of a dry electrode usually increases over time as more moisture permeates the skin–electrode interface resulting in increased coupling. On bare skin, dry electrodes normally exhibit higher contact impedances than wet electrodes by one order of magnitude difference [14]. However, with modern high-input impedance amplifiers, this is rarely an issue. As with wet electrodes, Ag/AgCl contact materials tend to show the best performance, especially in terms of drift noise, which is important for diagnostic ECG applications.

There are also dry-contact electrodes with capacitive coupling between the electrode and the body instead of coupling via galvanic conduction. Capacitive contact electrodes utilize a thin dielectric layer to form an insulated contact to the body. Compared to standard dry-contact electrodes, capacitive electrodes offer a galvanically isolated, chemically inert surface, maximizing user safety and electrode longevity. However, the capacitive interface precludes the measurement of true dc potentials and may result in long settling times depending on the bias resistor and the amount of coupling to the body. In other respects, the capacitive contact electrodes operate similar to dry-contact electrodes.

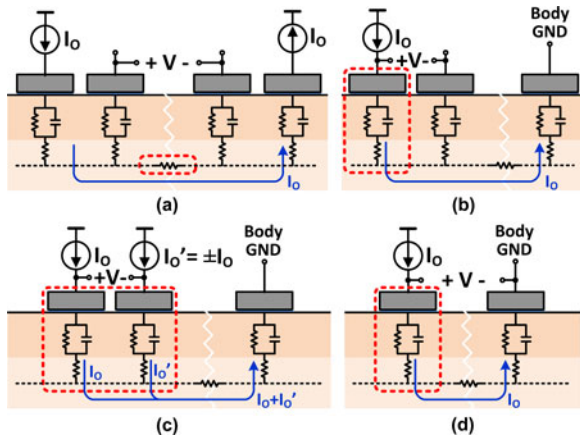


Fig. 3. Body–electrode interfaces for (a) EIT and (b)–(d) ETI measurements.

The final type of electrodes, noncontact, can be thought of as a special case of dry electrodes. They operate not only without gel, but also through an insulation layer such as clothing, enabling signal acquisition without direct skin contact. As expected, the coupling impedance can be very high on the order of tens of picofarad in parallel with hundreds of megaohm. Obtaining acceptable signals requires the use of special, very high input impedance active electrodes. Because there is no direct skin contact, movement artifacts are a major, unsolved issue especially for ambulatory use. Noncontact electrodes are also highly sensitive to environmental conditions such as humidity and the exact insulating material. Noncontact electrodes tend to work well on natural fabrics (e.g., cotton) under high humidity where the fabric actually becomes slightly conductive, offering a galvanic path to the skin. In contrast, it is difficult to obtain acceptable signals on high insulating synthetic fabrics (e.g., polyester) due to triboelectric artifacts.

B. Electrode Interfaces for Impedance Sensing

Controlled activation of current sources at electrode interfaces for biopotential sensing directly extends their use to sensing of electrical impedance. Two applications of impedance sensing are of particular interest: electrical impedance tomography (EIT) for medical imaging by spatial mapping of tissue impedance across body parts, and tissue–electrode impedance (ETI) checking for electrode contact quality monitoring.

EIT across a suitably sized array of electrodes placed over the body surface offers a low-cost, low-profile, noninvasive medical imaging modality free of ionizing radiation [15], [16] that has been applied to detection of breast cancer [17], imaging of brain function [18], [19], and monitoring of lung function [20]. A basic four-electrode setup for one EIT impedance element is illustrated in Fig. 3(a) [21]. High-impedance current sources inject complementary ac currents through two electrodes, while voltage is recorded between separate high-impedance sense electrodes. The recorded voltage is hence independent of any electrode impedance, and directly conveys tissue impedance between the body terminals interfacing with the sense electrodes.

A simple scheme for measurement of electrode–tissue impedance using three electrodes as shown in Fig. 3(b) has been implemented for the tracking of biopotential electrode quality and identification of movement artifacts [22], [23]. The voltage between one electrode driven by a high-impedance current source and another high input-impedance sensing electrode is measured to obtain only the electrode–tissue impedance connected to the ac current source [22]. Although activation of one ac current source can be interchanged between the two electrodes in order to measure both impedances in sequence, more reliable measurement is obtained by simultaneous activation of two equal magnitude ac current sources as shown in Fig. 3(c). The sum of electrode impedances is obtained from measurement of the voltage difference during activation of currents with opposing polarities, while the difference of impedances is obtained for same-polarity currents [24]–[26]. A simplified arrangement for directly estimating individual electrode impedance is shown in Fig. 3(d). This arrangement takes advantage of the availability of a low-impedance body ground connection and the fact that body tissue impedance is negligible in comparison to tissue–electrode impedance.

A standard driven right-leg (DRL) scheme with high-gain negative feedback between separate ground sense electrode and the drive ground electrode ensures that the body is at the system ground potential regardless of the injected electrode current [27], [28].

C. Optrode Interfaces for Spectrophotometric Sensing

Spectrophotometric measurement of blood oxygen saturation has been widely adopted in clinical and outpatient settings as it simultaneously provides information about heart rate, blood pressure variation, and respiratory function in a completely noninvasive modality at low power [30]. Light from two different light-emitting diodes (LEDs), at red (660 nm) and infrared (940 nm) wavelengths, is shined upon a body area with good perfusion, and quantification of either the transmitted or reflected light is done to calculate absorbance through the tissue by a photodiode. In this function, pulse oximeters are commonly presented as finger clips or rings and generally use transmission mode measurement, while more recent applications such as patches, wristwatches, and smartphones require a reflection-based system [31], [32] as shown in Fig. 4(a). Just like biopotential measurements, optical techniques can also be applied to quantify brain activity. Functional near-infrared spectroscopy (fNIRS) measures cerebral oxygenation, which is related to activity, through the skull [29]. fNIRS produces functional brain images from neighboring sources and detectors placed on the head as shown in Fig. 4(b). Distance and configuration of sources and detectors placement determines spatial resolution of the fNIRS. Recently, advances in integrated silicon avalanche photodiodes have dramatically improved the performance and wearability [33].

D. Problems and Challenges at the Interface

In addition to circuit noise from amplifier components, electrodes can be a significant noise contributor in the signal chain

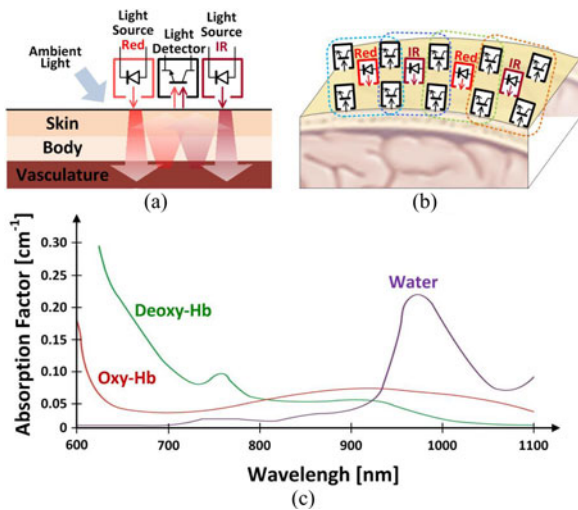


Fig. 4. Interface for (a) photoplethysmography and (b) functional near-infrared spectroscopy (fNIRS). (c) Absorption factors of oxyhemoglobin, deoxyhemoglobin, and water with respect to the light wavelength [29].

[9], [34]. Unlike circuit noise, however, comprehensive models for electrode noise do not exist, in part because the mechanisms for electrode noise are not well understood. In general, electrode noise is strongly correlated with the contact impedance but the actual level is significantly higher than the thermal noise from the resistive portion of the impedance.

The aggregate sum of the electrode noise sources can be quite large, in the order of $\mu\text{V}/\sqrt{\text{Hz}}$ at 1 Hz, even for wet electrodes. This far exceeds the noise contribution of circuit components, illustrating the importance of proper electrode selection. Due to integrated current noise, both wet and dry electrodes have sharp $1/f^2$ spectra, which shows up as baseline drifts in the time domain.

Noncontact electrodes can pick up additional noise from the insulating material between the metal and the skin. As an example, acquiring signals through fabrics can be noisy due to the intrinsic high resistance of the fabric ($>100\text{ M}\Omega$). This amounts to the equivalent of inserting a large resistor in series with the amplifier input and can add significant noise in the signal bandwidth.

Outside of controlled laboratory conditions, the largest noise sources will likely be electromagnetic interference (EMI) and movement artifacts. The most common symptom of EMI is seen as 50/60 Hz power line pickup. Triboelectric charging during subject movement is also a large, albeit less understood, source of interference. As a subject moves, the potential between the body and environment changes due to charge generation from striking the ground. This can couple into the system just like EMI and is often mistaken for movement artifacts induced by electrode–skin displacements.

EMI can be reduced or eliminated by a few simple techniques. Common-mode interference is easily attenuated through the use of a DRL circuit [27], [28]. This technique is well understood and operates by actively biasing the body potential toward a fixed circuit reference potential through the use of negative feedback. This has the effect of reducing the magnitude of common

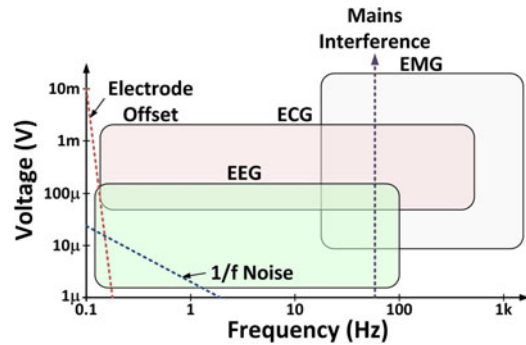


Fig. 5. Characteristics of EEG, ECG, and EMG, in relation to mains interference, electrode offset drift and $1/f$ noise [43], [44].

mode interference seen by the amplifiers. Differential pickup of EMI is mitigated through the use of active electrodes with an amplifier placed in close proximity to the electrode [35]–[39]. Alternatively, the use of shielded lead wires is also highly effective at accomplishing the same goal, minimizing the total area of high impedance traces that are susceptible to external electric fields [36].

Movement artifacts are a difficult challenge due to the lack of quantified metrics and clear design methodology. Any physical displacement between the electrode and the skin will necessarily generate noise, sometimes many orders of magnitude larger than the actual signal.

Movement artifacts can be eliminated by increasing the physical coupling pressure between the electrode and skin but may conflict with the need for comfort and wearability. Reducing movement artifacts highly relies on mechanical and industrial design, and solutions are highly dependent on the specific end application. In addition, electrode–tissue impedance measurement and signal processing techniques can be used to quantify and suppress movement artifacts [23]–[26], [40]–[42].

III. AFE FOR NONINVASIVE SENSING

A. Physiological Requirements

The main design requirements of the AFE, ASP, and ADC are driven by the characteristics of the physiological signals and the body–electrode interface.

1) *Biopotential Sensing*: Biopotentials, such as EEG, ECG, EMG, etc., are generated from volume conduction of currents made by collections of electrogenic cells. EEG is the electrical potential induced from collective activities of large number of neurons in the brain. ECG results from action potentials of cardiac muscle cells, and EMG from contractions of skeletal muscle cells. Various other biopotentials (EOG, ERG, EGG, etc.) also result from collective effects of large numbers of electrogenic cells or ionic distribution.

Almost all biopotentials, including EEG, ECG, and EMG, of which characteristics are shown in Fig. 5, range over very low frequency, typically less than 1 kHz. They are very low in amplitude ranging tens to hundreds microvolt when measured by a surface electrode. Since EEG and ECG range down to less than 1 Hz, recording of these signals faces challenges in electrode

TABLE II
DESIGN FACTORS AND TRADEOFFS IN INTEGRATED ELECTRODE INTERFACES FOR NONINVASIVE PHYSIOLOGICAL MONITORING

Design Factors	Trade-Offs and Inter-Relations	Typical Range (Biopotentials)	Examples	Comments
Input Referred Noise		1–5 μV_{rms}	[64, 65, 69]	Dominated by electrode interface and front-end amplifier
Power Consumption		0.1–100 μW	[60, 64, 65]	Lowered by biasing, or duty cycling/multiplexing above Nyquist rate
Bandwidth		0.1–10 kHz	[57, 63, 65]	Application specific or configurable
Dynamic Range (DR)		40–120 dB	[39, 63, 65]	Variable gain compounds signal-to-noise ratio for extended DR
Variable Gain		1–1,000 V/V	[60, 63, 65]	Typically digitally selectable with auto-ranging capability
Power Supply Rejection Ratio (PSRR)		40–80 dB	[22, 63, 75]	Frequency dependent, limiting switching regulator frequency
Common-Mode Rejection Ratio (CMRR)		60–120 dB	[22, 63, 64]	Mostly mains interference rejection; through active grounding (DRL)
Input Impedance		100 M Ω –10 T Ω	[12, 39, 67]	Resistive/capacitive; depending on the contact type and application
DC and Low-Frequency Rejection		0.1–1 Hz	[56, 66, 67]	AC coupling; with CDS or chopping for $1/f$ noise and offset reduction
Movement Artifact Rejection			[23, 41, 42]	Mostly reduction of relative motion through mechanical restraint
Area / Size		0.1–10 cm^2	[22, 39, 71]	Dominated by electrodes and battery; minimizing off-chip components

▲: factors to be maximized; ▽: factors to be minimized.

offset voltage, which may reach up to 100 mV, varying slowly over time. In addition, $1/f$ noise needs to be suppressed if the application calls for low noise at low frequencies (<1 Hz). Also, common-mode interference from the mains and other irrelevant biopotentials should be sufficiently rejected.

2) *Electrode–Tissue Impedance Measurement*: The measurement of electrode–tissue impedance (ETI) is implemented by sensing a potential between electrodes while injecting an alternating current. Therefore, most of the requirements for biopotential sensing also apply to ETI measurement circuit. However, in order to identify and suppress movement artifacts, the electrode–tissue impedance and biopotential signal should be sensed simultaneously [23], [24]. This requires chopper stabilization schemes for the impedance measurement to separate electrophysiological from resistive and reactive impedance signals, each occupying different frequency bands (see Section III-H).

As additional advantage, chopper stabilization shields the electrode from any dc currents, such as caused by imbalances between source and sink currents and which lead to harmonic distortion and saturated outputs [26]. The high dynamic range of kilohm range electrode–tissue impedances amidst ohm-range body tissue impedances [45], could further be a potential source of saturation, mitigated by varying the amplitude of the ac current. Larger injected ac currents lower the input-referred noise at the expense of power.

3) *Optics-Based Sensing*: Pulse oximeters and fNIRS systems have similar system requirements. The bandwidth of the hemodynamic and oxygenation signals ranges from approximately dc to 20 Hz. However, it is preferable to sample these signals at greater than 240 Hz, the Nyquist frequency of fluorescent light, to prevent aliasing of 60-Hz background interference [31]. Light attenuation is in the range of 10^{-4} – 10^{-3} , with reflection-based systems showing greater attenuation than transmission systems [46]. The ac/dc contrast ratio can be as low as 0.25–1% of which accuracy must be within 2% [30]; thus contrast detection in front-end system must have a resolution of around 0.01% while being able to reject a large range of dc light incidence due to the variability in application (patients, environment, movement artifact, etc.). Peak LED driving currents for pulse oximetry are in the few tens of microampere range and the duty cycle for the low-power pulsed system can be as low as 1–3% [46], [47]. The light source to detector distance is

approximately 3 mm in reflection oximetry systems [32], while in fNIRS this separation must be around 3 cm to be able to image the cerebral cortex noninvasively [48]. Additionally, fNIRS systems require higher CMRR to reject interference [49].

B. Design Factors, Interrelations, and Tradeoffs

Several factors quantifying the metrics of performance and cost in the design, their interrelationships, and typical ranges from the literature, are summarized in Table II. Several of these relationships, such as between noise, power, bandwidth, gain, and dynamic range are generally well understood deriving from fundamental physical and information theoretic principles, e.g., power is typically linear in bandwidth but subject to noise considerations. Other relationships, such as between input impedance and movement artifact rejection, are specific to the physiological signals and environmental factors at the electrode interface. The various intertwined relationships between these factors must be cooptimized in the design tradeoffs at the electrode, circuit, and architectural levels. A deep understanding of fundamental principles linking these factors and driving the tradeoffs is thus required. Specific tradeoffs and architectural design topologies that take advantage of properties of low-power CMOS integrated circuits and systems are elaborated in the following sections.

C. Subthreshold Operation of MOS Transistors

Counter to standard practices in analog CMOS circuit design, the weak inversion (subthreshold) region of CMOS operation has proven a favorable regime for low-power biomedical circuit design. In conventional design, particularly for high-speed applications, weak inversion operation has been considered as nonideality in a cut-off region and its current has been labeled as leakage current. Recently, weak inversion has become increasingly important because its low-power and low-bandwidth characteristics are well suited for biomedical and other low-power sensor applications, owing to superior transconductance efficiency. Also, it does not suffer from many process-dependent problems plaguing the above-threshold region in deep submicron technology, such as gain-limiting effects of velocity saturation in electron and hole mobility [50].

Transistor model equations in weak inversion are simpler, more transparent, and scale over a wider range than in strong

inversion. The electron energy of a transistor in weak inversion is based entirely on the Fermi–Dirac distribution, independent of process technology. The drain current through the transistor channel flows not by drift, but by diffusion, and changes exponentially with gate voltage [30]. Drain current i_{DS} , transconductance g_m , and unity-gain frequency f_t in weak inversion are as follows:

$$i_{DS} = i_{DS0} \frac{W}{L} e^{v_{GS}/(nV_t)} \left(1 - e^{-v_{DS}/V_t}\right) \quad (1)$$

$$g_m = \frac{I_{DS}}{nV_t} \quad (2)$$

$$f_t = \frac{I_{DS}}{2\pi nV_t (C_{gs} + C_{gd} + C_{gb})} \propto I_{DS}. \quad (3)$$

Because the transconductance is linearly proportional to drain current, so is the unity-gain frequency. Thus, the tradeoff between current and bandwidth is very straightforward: the larger the current, the wider the bandwidth.

Thermal noise in saturation and weak inversion is proportional to drain current as follows [51]:

$$\overline{i_{n,th}^2} = 2q\overline{I_{DS}}\Delta f \quad (4)$$

where Δf is the signal bandwidth. The relative noise power (inverse of the signal-to-noise ratio) is inversely proportional to drain current:

$$\frac{\overline{i_{n,th}^2}}{I_{DS}^2} = \frac{2q\Delta f}{I_{DS}}. \quad (5)$$

Therefore, the signal-to-noise ratio is linearly proportional to bias current in weak inversion. For a majority of biomedical applications with narrow signal bandwidth, the lower currents of circuits in weak inversion still offer adequately large signal-to-noise ratio at maximum energy efficiency.

Flicker noise, also known as $1/f$ noise or pink noise, is also a significant noise source at low frequency. Random captures of carriers in traps near the Si/SiO₂ interface and some other mechanisms are known to be a main source of $1/f$ noise [52], [53]. PMOS transistors are known to have less $1/f$ noise than NMOS transistors, and therefore should be used in the input differential pair of a front-end amplifier for low-noise low-frequency applications in biosensing. Enlarging the MOS device size also decreases $1/f$ noise inversely proportional to area. For low-noise biomedical applications such as EEG acquisition, the chopper stabilization technique is widely used to reduce $1/f$ noise further (see Section III-F). Other techniques such as auto-zeroing and correlated double sampling can be used to reduce $1/f$ noise as well [54].

D. Instrumentation Amplifier Design

One of the most challenging parts in the design of a wearable physiological monitoring system is the implementation of instrumentation amplifiers (IAs), which acquire biosignals from electrodes and perform analog signal processing and conditioning. IAs are subject to almost all the challenging design specifications aforementioned in Section III-B.

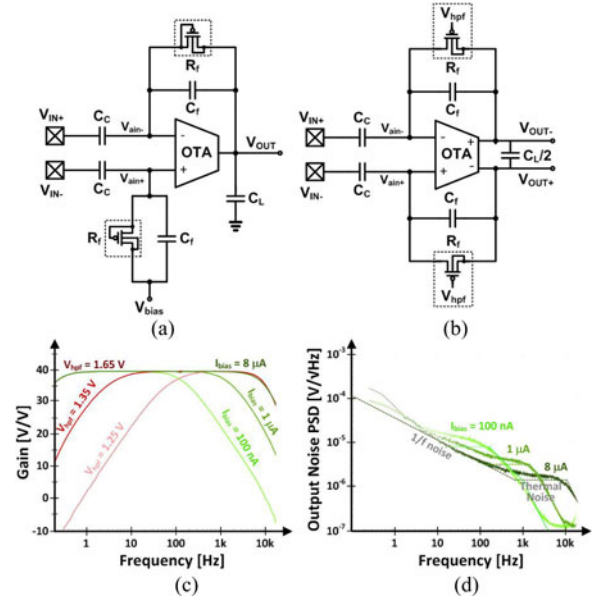


Fig. 6. Generic architectures of (a) single-ended output [56] and (b) fully differential instrumentation amplifiers. Measured (c) transfer function and (d) output noise power spectral density for different configuration settings of the OTA bias current I_{bias} and pseudoresistance voltage bias V_{hpf} [57].

A classic three-opamp IA is adequate for achieving large input impedance, large CMRR, and sufficient gain. However, it consumes large power and area [55] since it uses three amplifiers. For a micropower biopotential acquisition front-end, the configurations shown in Fig. 6(a) (similar to [56]) and (b) (similar to [57]) are widely used. The ac-coupling input capacitors C_C block electrode offset voltages. Owing to favorable matching performance of capacitors in integrated CMOS processes, the gain can be precisely controlled. A large resistor R_f , typically implemented by a pseudoresistor or a switched-capacitor circuit (see Section III-E), establishes dc biasing of the voltage at the input nodes of the amplifier and performs high-pass filtering together with C_f . Mismatch in capacitor values results in the degradation of the CMRR. A practical CMRR that this architecture can achieve is about 60 to 70 dB. In addition, C_C dominates the input impedance. Therefore, the value of C_C needs to be set by considering CMRR and the input impedance.

The passband gain is determined by the ratio of capacitors C_C to C_f . The high-pass cutoff frequency is set by the product of R_f and C_f . The low-pass cutoff frequency is approximately $g_m C_f / 2\pi C_C C_L$, which can be controlled by the load capacitor C_L . The right-half-plane zero at g_m / C_f can be canceled by inserting a $1/g_m$ resistor in series with C_f . However, it can be ignored in many cases because it is located at much higher frequency than the frequency range of interest for biomedical applications.

The main noise contributors of the single-stage IAs are the operational transconductance amplifier (OTA) and the feedback resistor R_f . In practical circuits, the noise from the OTA is dominant over the noise from R_f [58].

As a benchmark in the design of front-end IAs for low noise and low supply current, the noise efficiency factor (NEF) is used

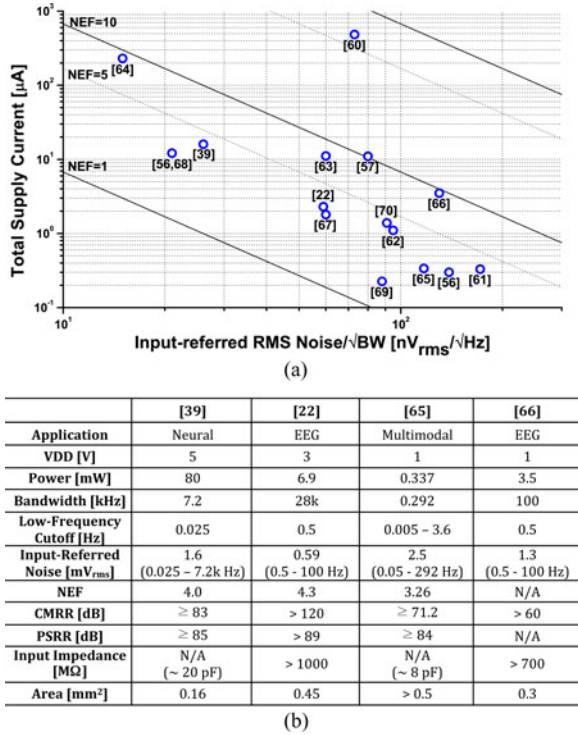


Fig. 7. (a) NEF and (b) performance summary of state-of-the-art IAs for noninvasive biomedical applications.

to compare the current-noise performance:

$$NEF = V_{\text{rms},\text{in}} = \sqrt{\frac{2I_{\text{tot}}}{\pi V_t \cdot 4kT \cdot BW}} \quad (6)$$

where V_{rms} is the total input-referred noise, I_{tot} the total current drain in the system, V_t the thermal voltage, and BW the -3 -dB bandwidth of the system [59]. The NEF corresponds to the normalized supply current relative to that of a single BJT with ideal current load for the same noise level, defining the theoretical limit ($NEF = 1$). In practice, differential IAs with input differential pairs incur twice the supply current for the same transconductance, with NEF values greater than 2. The state-of-the-art IAs typically have NEF of 2.5 to 10. As a point of reference, measured NEF and performance of state-of-the-art IAs are shown in Fig. 7(a) and (b), respectively, [22], [39], [56], [57], [60], [61]–[70].

Note that even though NEF is widely used to benchmark IAs, NEF is nothing more but a tradeoff between only three performance metrics: bandwidth, noise, and current—excluding many other critical performance factors such as CMRR, input impedance, power consumption, input dynamic range, etc. Modified NEF metrics, one comparing power consumption instead of current [71], and another including power consumption and dynamic range [72], have been proposed as more comprehensive NEF alternatives.

E. Pseudoresistors for Subheartz High-Pass Cutoff

The high-pass cutoff frequency needs to be well below 1 Hz in typical biomedical sensors, requiring ultrahigh resistance in the

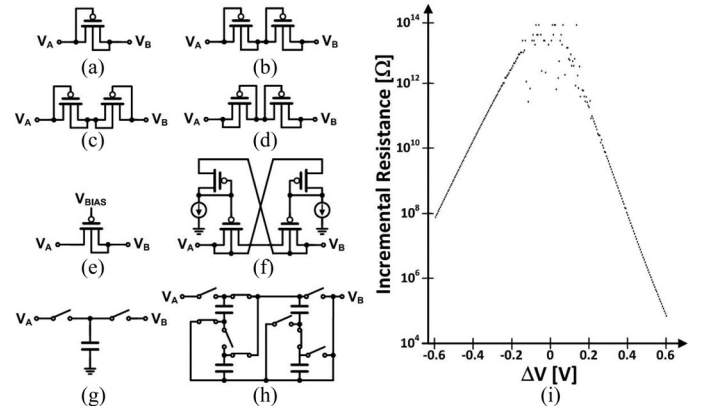


Fig. 8. On-chip pseudoresistor implementations: (a) single MOS-bipolar pseudoresistor [73], (b) pseudoresistor with two MOS-bipolar elements in series for twice higher resistance and greater voltage range [56], [74], (c) symmetrical version with outwardly connected gates, (d) symmetrical version with inwardly connected gates [39], [61], [75], (e) voltage-biased pseudoresistor for resistance tunability [57], [72], [76]–[78], (f) balanced tunable pseudoresistor with wider linear range [65], (g) switched-capacitor implementation [62], (h) switched-capacitor implementation with 10-times larger effective resistance than (g) [66]. (i) Measured resistance of a single MOS-bipolar pseudoresistor (a) as a function of voltage [56].

teraohm range. Realizing subheartz time constants with on-chip capacitors and poly resistors consumes an impractically large area for integrated implementation.

The most prevalent solutions are combinations of 1–10 pF capacitors with PMOS-based MOS-bipolar pseudoresistors as shown in Fig. 8(a)–(f) [56], [73]. The most basic topology among these is a PMOS whose gate and body terminals are connected as Fig. 8(a) [73]. This PMOS pseudoresistor combines a pn-junction in the forward direction ($V_A > V_B$) with a diode-connected subthreshold PMOS in the reverse direction ($V_A < V_B$). Owing to the source-bulk connection, the gate-connected drain terminal is leakage free and is ideally connected to a leakage-sensitive side such as a floating input to an OTA. The measured resistance of a single MOS-bipolar pseudoresistor is shown in Fig. 8(i) [56]. A configuration with the PMOS gate connected to a bias voltage in Fig. 8(e) results in a controllable resistance by gate voltage [57], [72], [76]–[78]. However, the resistance of the PMOS-based pseudoresistors in Fig. 8(a)–(e) drops drastically when the voltage across moves away from zero, inducing signal-dependent distortion while limiting the voltage dynamic range [65]. The pseudoresistor in Fig. 8(f) has balanced resistance with wider linear range up to a few hundred microvolt. An even wider linear range can be achieved by using an auxiliary amplifier [79].

However, standard MOS-bipolar pseudoresistors suffer from process, voltage, and temperature (PVT) variations in addition to possible light and EMI sensitivities, leading to variations in cutoff frequency. Switched capacitors can be used to implement on-chip PVT-insensitive high resistance as shown in Fig. 8(g) [62]. In this topology, the switching frequency f_s and the capacitor in the middle determine the resistance precisely as $1/f_s C$. The switched-capacitor resistor in Fig. 8(h) mitigates manufacturability and interference issues by realizing a tenfold

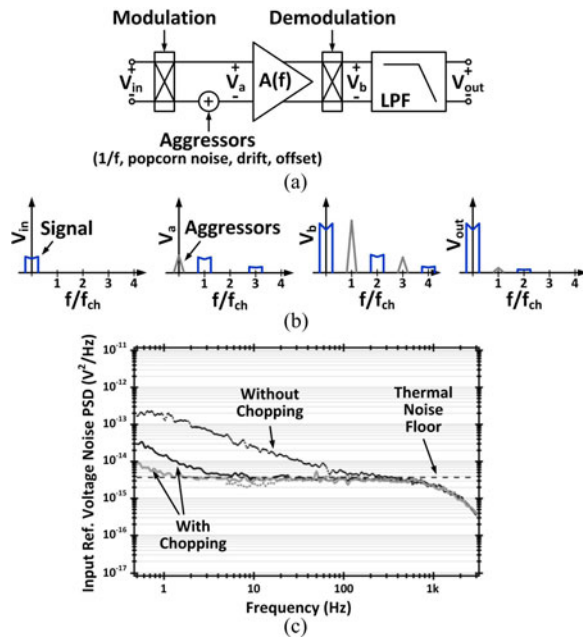


Fig. 9. (a) Block diagram and (b) frequency-domain illustration of the chopper technique for low-frequency noise and drift cancellation [54], [83]–[85]. (c) Input-referred noise spectrum with and without chopping [63].

resistance increase by charge sharing in the switched-capacitor circuits [66].

F. Offset and $1/f$ Noise Cancellation Techniques

Autozeroing switched-capacitor techniques are often used to suppress electrode voltage offset and $1/f$ noise of the amplifier [54]. However, opening of the reset switch on the sampling capacitor after autozeroing introduces significant Nyquist–Johnson noise (kT/C noise) [80], [81] and random charge injection that contaminate the sampled signal. The kT/C noise of a 1–10 pF capacitance alone is about tens of microvolt. To resolve this noise issue referred to the input of the AFE, signal folding and digital-assisted signal stitching can be used, resulting in relieving the specification of voltage dynamic range [82]. Instead, almost all of the IAs utilize chopper stabilization techniques to obviate $1/f$ noise.

1) *Chopper Stabilization Techniques*: The chopper modulation technique is widespread and essential to mitigate $1/f$ noise and other low-frequency noise, such as popcorn noise, voltage offsets, and drifts, for EEG and other low-noise ($< 1\text{--}2 \mu V_{\text{rms}}$ input-referred noise) biopotential acquisition. The principles of the chopper modulation technique for amplifiers, which have been extensively studied [54], [83]–[85], are illustrated in Fig. 9. The low-frequency band-limited input signal V_{in} is modulated in front of the amplifier by a square-wave chopping signal. The resulting waveform V_a for the signal is shifted to the chopping frequency f_{ch} , and the aggressors do not fall within the signal band. After the amplification and demodulation with the same chopping signal, the amplified input signal components are shifted to dc baseband frequency at V_b while the aggressors are moved to f_{ch} outside of the signal band. All the undesired aggressors and the harmonics are filtered out through the low-

pass filter, and the desired input signal is ideally restored at the output V_{out} .

The residual offset is mainly caused by the nonidealities of the input chopper modulator. The mismatch of the clock-feedthrough and the charge injection in the input chopper generates switching transient spikes, which are demodulated at the output chopper into a residual output offset. In order to minimize the offset, at first, careful design and layout need to be done. A continuous [22], [62], [64], [66] or digital [39] dc servo loop can reduce the residual offset, and mitigate the signal distortion problem that is caused by the finite bandwidth of the amplifier. Alternatively, filtering techniques [63], [86], [87] can be applied. Output ripple is induced by the input offset of the amplifier, and can saturate the output of the amplifier since offset is also amplified. The ripple can be reduced by a continuous ripple-reduction loop [64] and a digital foreground calibration [39].

G. CMRR Enhancement Techniques

Common-mode interference is a difficult challenge for biomedical signal sensing systems. The major source of the interference comes from electric power lines, which are electrically coupled to the human body. A high CMRR is required in the system to reject the common-mode interference in order to ensure high signal quality.

Accurate component matching between differential signal lines and between the channels is the most fundamental requirement to accomplish high CMRR. Good matching involves techniques from careful layout to smart architectural design choices.

1) *DRL Technique*: The DRL technique feeds the amplified input common-mode voltage into the body through an additional electrode, which has been placed on the right leg for ECG measurements. This negative feedback reduces the impedance in the feedback loop, attenuating the common-mode interference voltage at the sensor inputs [27], [28] by factor of the feedback loop gain. Through the DRL negative feedback, the electrode impedance and common-mode voltage are reduced by the factor of the DRL loop gain. Hence in order to obtain higher gain, an open-loop DRL amplifier can be employed [88]. Digitally-assisted DRL circuits offer larger gain at the mains frequency for higher rejection and lower gain elsewhere for stability [89]. In dry-electrode applications, common-mode feedback to the negative inputs of individual amplifiers on the active electrodes also increases CMRR, and ensures stability unaffected by electrode impedance variations [39].

2) *Input Impedance Boosting Techniques*: The variation and mismatch of electrode impedances also degrade the CMRR, reduce signal amplitude, and make the system more susceptible to movement artifacts. Thus, the input impedance of the biopotential sensor should be much higher than the electrode impedance and the interface impedance between the body and the electrode. A positive feedback can bootstrap the ac-coupled input capacitors to boost the input impedance [23], [39], [67], achieving input impedance in the order of gigaohm. In order to further boost input impedance to the teraohm level, a unity-gain amplifier

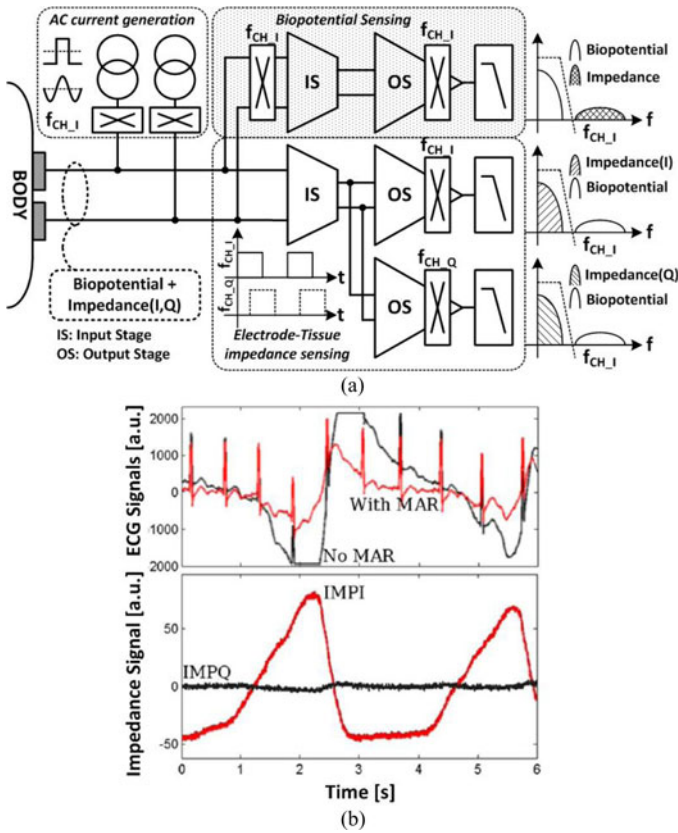


Fig. 10. Electrode-tissue impedance measurement concurrent with biopotential recording. (a) Periodic current injection and synchronous detection of resistive and reactive components of impedance along with the chopped biopotential signal. (b) Movement artifact reduction in an ECG signal through linear correction with the estimated impedance signals [23].

with active shielding can be used to bootstrap capacitance of the input transistor and all other parasitic capacitance [12].

H. Impedance Measurement

Movement artifacts can be suppressed by sensing electrode-tissue impedance and biopotentials simultaneously. In Fig. 10(a), an ac current generation block with a chopper injects ac current into the sensing electrodes [23]–[25]. Due to the electrode-tissue impedance, voltage signals including the impedance information are superimposed on the original biopotentials. Note that the electrode-tissue impedance has resistive and capacitive components resulting in real and imaginary components, respectively. All signals are directed to readout circuits. To separate biopotential and impedance signals, only the IA for biopotentials has a chopper at its input. For distinguishing real and imaginary parts in impedance signals, the output chopper blocks use two phases in quadrature, f_{CH_I} and f_{CH_Q} . The IA with f_{CH_Q} projects the voltage response corresponding to the electrode reactance into the low-frequency band while other signal components are either canceled or projected to high frequencies and subsequently rejected by low-pass filters, such that only signals in low-frequency band are shown at the output [23]–[25].

A purely sinusoidal current generator for impedance probing without a chopper block is reported in [90]. Due to large power

consumption of the sinusoidal ac current source, a simple pulse-wave current source is implemented in [22], [24], and [25]. However, since a pulsed current contains large higher harmonics that get folded into baseband, it leads to 23% measurement error. To avoid large power consumption and harmonic distortions, a 16-level quantized-sinusoidal current source is proposed in [45].

The sensed signals by the circuit structure in Fig. 10(a) are the input of an adaptive filter with an LMS algorithm [24], [26]. Fig. 10(b) clearly shows that this method is able to reduce the effect of movement artifacts with the estimated impedance signals shown in Fig. 10(c) [23].

I. Optics-Based Sensing

Pulse oximetry is accomplished by spectrophotometric measurement of the relative absorbances of arterial blood to red and infrared light. The absorbance of the background tissue and other interferences is rejected by sampling several times throughout the period of a heartbeat, while the amount of blood that perfuses the probed area varies. The actual physical quantity observed is the ratio of the red over the IR contrasts, where contrast is defined as the quotient of the ac amplitude over the dc magnitude of the current generated at the photodiode for each color. Once this ratio is computed, blood oxygen saturation can be computed with a simple formula [30]. The general architecture of a pulse oximeter includes a probe, a photoreceptor, analog signal conditioning, and a digital processor and controller [46]. The probe consists of the two LEDs that generate the monochromatic signals, along with drivers, switching and pulse modulation circuitry. The photoreceptor consists of a photodiode to sense the incoming light and a transimpedance amplifier (TIA) to amplify and convert the current driven by the sensor into a voltage. Consequently, analog low-pass filtering removes artifacts from the switching and pulsing of the probe light, which is generally much faster than the pulse signal of interest. Finally, the ratio between the red and IR signals (which can come in parallel channels) can be computed in analog domain before digitization.

Integrated circuit advances in photoplethysmography have dramatically decreased the power consumption of these devices. An ultralow power version of a whole system can consume 4.8 mW, or last 60 days on 4 AAA batteries [47]. This is possible by reducing the duty cycle of the probe LEDs, by an innovative logarithmic TIA with adaptive filtering and gain and by analog ratio computation. Imaging brain activity with fNIRS systems has a similar architecture with pulse oximetry. Advances include integration of silicon avalanche photodiodes in the photoreceptor IC, along with a linear TIA for very low noise and high gain detection [33]; and improvements in the spatial and temporal resolution of multichannel systems by code-division-multiple-access modulation of different emitters and detectors [48].

IV. SIGNAL CODING AND DIGITIZATION

Digitization of the recorded and processed analog physiological signals is required for further digital signal processing and digital RF communication. The tight power and low noise constraints demand ultralow power ADCs at low-frequency range

(1–10 kHz) without sacrificing noise performance, while requiring no or very little static current drain and scalable power consumption with respect to sampling rate for multimodal recording applications. Both successive-approximation ADC and oversampling $\Delta\Sigma$ ADC are superior architectures for achieving the specifications with lowest power dissipation.

A. Successive-Approximation ADC

Successive-approximation register (SAR) ADC is the dominant architecture for low-power medium-resolution (8–12 bits) biomedical applications due to its simple architecture involving few analog circuits and its low-power consumption at low frequency without static power consumption [22], [23], [65], [70], [91]–[95]. Successive approximation of the sampled input performs a binary search over the input range using a time-multiplexing switched-capacitor digital-to-analog converter (DAC) based on iterative partial one-bit quantization results in the order from the most significant bit to the least significant bit [96], [97].

Several techniques and architectures can be applied to minimize the power consumption of the SAR ADC. Using a main and subbinary weighted DAC arrays with a series attenuation capacitor can reduce the total size of the capacitor array; leading to reduced power consumption in the ADC driver and also in the capacitor DAC [98]. Also, the folded capacitor DAC architecture with divided reference voltages reduces the size of capacitor DAC, resulting in further power saving [92]. Using charge-recycling switching methods results in further power savings in the switching of the capacitor DAC [99].

SAR ADCs are generally considered to be most energy efficient for medium-precision low-sampling-rate digitization. However, most micropower SAR ADCs operate at signal levels substantially (3–4 orders of magnitude) greater than typical signal level of physiological signals (see Fig. 5). They require significant amplification before analog-to-digital conversion for submicrovolt resolution. Furthermore, sampling at the Nyquist frequency demands substantially more stringent antialiasing analog filtering than required using oversampling techniques. The cost of amplification and antialiasing filtering are often not accounted for in ADC energy metrics. Most critically, sampling of biosignals at microvolt resolution is problematic due to kT/C sampling noise on capacitors which may amount to several tens of microvolt for typical picofarad-range capacitors in integrated circuits.

B. $\Delta\Sigma$ Oversampling ADC

$\Delta\Sigma$ ADCs are an alternative solution with the following strengths [57], [100]–[103]: 1) Resolution and sampling rate can be dynamically reconfigured, with sampling rate proportional to power consumption, so they are adequate for multimodal biopotential sensor applications; 2) they require only few and simple analog components; 3) they are suited for low-power and low-voltage operation; 4) they easily achieve 12–16 bits or higher resolution without complex circuit and layout techniques; 5) continuous-time $\Delta\Sigma$ topologies are free of kT/C sampling noise and less subject to aliasing and noise folding.

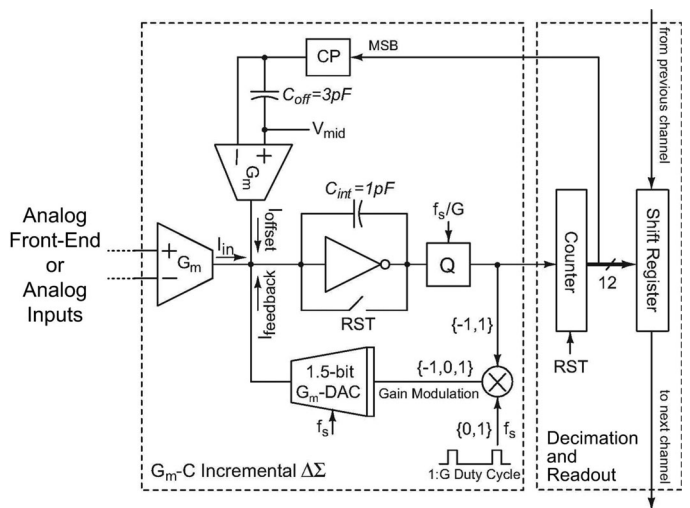


Fig. 11. Oversampling, aliasing-free biopotential acquisition system utilizing Gm-C incremental $\Delta\Sigma$ ADC [57].

A Gm-C incremental $\Delta\Sigma$ ADC with widely configurable resolution and sampling rate is shown in Fig. 11 [57]. A transconductance (G_m) cell converts the differential input voltage signal to a current, approximately linear over the voltage range of typical biopotentials. The difference between this current and a feedback current is integrated and the resulting voltage is compared for three-level quantization of the feedback current, implementing a continuous-time first-order $\Delta\Sigma$ modulator. A continuous-time oversampling ADC avoids the need for antialiasing filter and sample-and-hold circuits preceding the ADC. In addition, direct digital control over the duty cycle in the feedback offers precise digital gain programmability from 1 to 4096.

Another example incremental $\Delta\Sigma$ ADC for noninvasive biopotential recording is given in [100]. It receives unbuffered biopotential signals and performs amplification, signal conditioning, and digitization using only a single OTA. Other alternative ADC architectures include a hybrid architecture of SAR and $\Delta\Sigma$ ADC [101], asynchronous level-crossing ADCs [104], [105], and a bioinspired ADC with the successive integrate-and-fire operation [106].

The performance of ADCs can be measured and compared by the Walden figure of merit (FOM), which quantifies energy consumed per conversion step as $\text{Power} / (2^{\text{ENOB}} f_s)$. Fig. 12 shows this FOM for all major ADCs reported from 1997 to 2013 [107] including ADCs for noninvasive physiological monitoring systems. [65], [72], [91], [92], [98], [101], [103], [104], [106], [108]–[110].

C. Application-Specific Signal Encoding

Digital signal processing (DSP) compressed encoding of the digitized data prior to RF wireless transmission may lead to substantial energy savings, particularly in high-dimensional or high-bandwidth physiological sensing applications where the amount of useful information is significantly lower than the data rate requirements of the raw signals. For example, in EEG sensing for epileptic seizure detection [66], [70], 18 electrodes

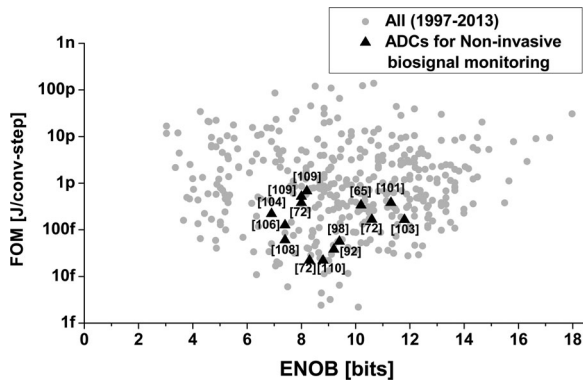


Fig. 12. FOM versus ENOB of the state-of-the-art ADCs for biomedical applications.

produce 200-Hz 12-bit data resulting in a total data rate of 43.2 kb/s. Employing digital processing for feature extraction and seizure detection reduces this data bandwidth to 2 kb/s with a ten-fold reduction in power dissipation [66].

Equally importantly, energy-efficient analog preprocessing can lead to significant reduction of data bandwidth and power in the ADC in addition to the RF block. A low-power ADC and digital blocks can substitute a high-performance ADC and digital signal processor. For example, typical EEG/ECOG-based brain-computer interface (BCI) applications do not need raw data, but spectral characteristics of the recordings. Thus, extracting spectral power of the required frequency bands in the AFE can reduce power dissipation and/or complexity in the ADC, DSP, and RF blocks [75]. Other applications of analog and mixed-signal preprocessing for low-power high-performance biosignal processing include ECG physiological monitoring systems for efficient QRS detection and coding [25], [95].

V. SYSTEM EXAMPLES

Examples of complete noninvasive physiological monitoring systems covering a range of cardiac, respiratory, muscular, and brain activity signals under a variety of environmental conditions, including underwater and noncontact sensing, are given below. Application-specific design of the electrode interfaces contribute to extend the applicable scope to ambulatory monitoring outside of the hospital.

A. Noncontact ECG Bed

One highly promising application of noncontact capacitive electrode interfaces is ECG monitoring embedded in beds [111]–[114]. Integration of electrodes underneath a commercial bed sheet (e.g., Fig. 13) enables noncontact electrode coupling, through thin common nightwear, to a subject lying on the bed. This implementation relieves the user not only of skin irritation but also of cumbersome electrode attachment, connecting to ambient health monitoring and increased patient compliance for every night use. Combined monitoring of ECG with breathing activity also extends the application area to neonatal supervision [115], [116] and sleep apnea screening. The breathing

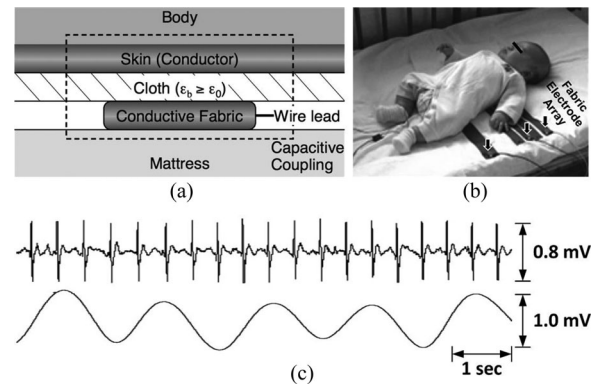


Fig. 13. Example of noncontact electrode interface for monitoring ECG and breathing on bed. (a) Fabric electrode placed on a bed and coupled indirectly to the skin [112]. (b) Fabric bed electrodes placed on a bed for monitoring ECG and breathing activity [111]. (c) Signal recording of narrow-band ECG (top) and simultaneously measured breathing activity (bottom) [115].

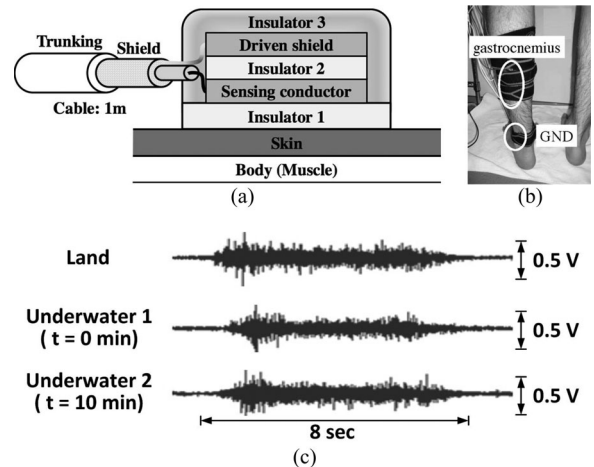


Fig. 14. Example of insulated electrode interface for measuring underwater EMG. (a) Schematic of electrode configuration coated wholly with hydrophobic insulator, (b) electrode placement, and (c) measured EMG signal from gastrocnemius muscle during plantar flexion with the electrode in (a) [117].

signal is obtained by capacitive sensing of displacement using the same capacitive coupling electrode used for ECG sensing.

B. Underwater EMG Sensing

Another novel application of the insulated capacitive electrode interface is underwater EMG monitoring [117]. Coating the electrodes with a thin water-proof insulating material (e.g., Fig. 14) prevents them from short-circuiting due to ions in water, and hence enhances the selectivity of the electrode coupling to the physiological voltage source (i.e., muscles in [117]) even in the case where the target source is immersed in conductive liquid.

C. Wearable ECG and EEG Systems

Mobile applications of wireless noninvasive physiological sensing include wearable systems for continuous ambulatory biopotential monitoring, made possible by advancements in electronics miniaturization, low noise dry sensors and innovative

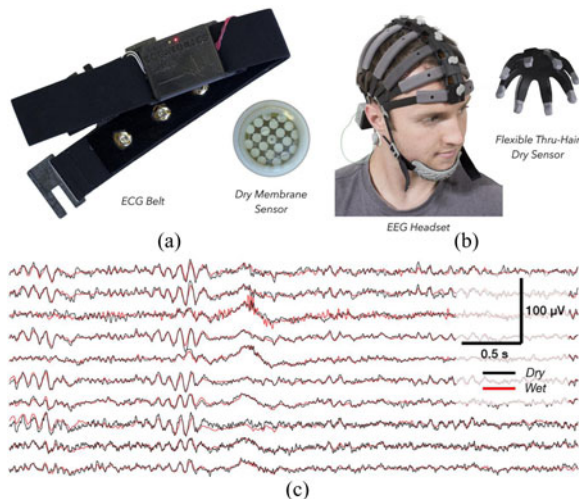


Fig. 15. Examples of wearable dry electrode systems. (a) Dry-contact ECG belt with low noise membrane-based sensor [118]. (b) High-density dry EEG headset with flexible electrodes that can operate through hair [10]. (c) Simultaneous recording between wet (Ag/AgCl conductive gel) and the dry EEG headset showing the high signal quality [10].

mechanical form factors. Fig. 15 show two examples of ECG and EEG systems.

The ECG belt utilizes a linear array of membrane-based dry-contact sensors. Unlike conventional metal-based electrodes, the membrane signal utilizes a semipermeable surface which encapsulates a hydrogel. The membrane allows for ionic conduction between the body, through the membrane and into the hydrogel. This buffers the electrochemical interface by providing a stable gel-metal layer away from the skin and reduces the sensor noise [118].

For EEG, head hair presents a challenge for dry electrodes which must reach the scalp. A flexible electrode is made from an elastomeric material which bends to brush aside hair and avoids the need for hard metallic prongs. An array of flexible sensors (up to 64) is placed within a mechanical headset that is adaptable to variety of head shapes and sizes. All of the AFE, ASP, ADC, DSP, and RF electronics are integrated onto the headset enabling mobile EEG acquisition [10].

VI. CONCLUSION

The advent of ubiquitous wearable physiological monitoring promises to reduce some of the rising healthcare costs affecting developed and developing nations. Customized applications bring opportunities for better preventive care and increasing public awareness of their own medical conditions. In this paper, we focused on the integrated circuit techniques to improve the performance and expand the applications of noninvasive physiological monitoring instrumentation and discussed the challenges at the electrode–body interface. From these interface considerations, we developed system requirements for reliable signal acquisition in biopotential, electrode–tissue impedance, and spectrophotometric measurements. Some of the main techniques for implementing CMOS subthreshold integrated instrumentation amplifiers in a low-noise and power-efficient manner were

covered: pseudoresistors, chopping, driven right-leg circuits, impedance bootstrapping, and application-specific design for electrode–tissue impedance measurements and photoplethysmography. Highly efficient data conversion and signal encoding for digital transmission were also reviewed. Finally, examples of wearable and unobtrusive systems for physiological monitoring in novel applications were presented. These innovations, and others to come in the next decade, will continue to benefit from interdisciplinary collaborations between developers and users of the noninvasive physiological monitoring technology such as new physiological signal modalities, innovative electrode interfaces, improvements in integrated circuit design methodologies and silicon technologies, improved system-level design optimizing for human factors and ergonomics, and clinician and patient perspectives on medical diagnostics and personal healthcare.

ACKNOWLEDGMENT

The authors would like to thank M. Mollazadeh, E. Greenwald, and N. Thakor for collaborations on neural and cardiovascular electrophysiology systems, Y. Fukuoka for analysis of indirectly measured ECG and EMG signals, and T. Kerth for contributions to design of and experiments with the Cognionics 64-channel wireless dry EEG headset.

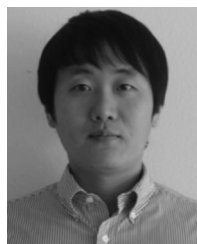
REFERENCES

- [1] A. Lopez and P. C. Richardson, "Capacitive electrocardiographic and bioelectric electrodes," *IEEE Trans. Biomed. Eng.*, vol. BME-16, no. 1, p. 99, Jan. 1969.
- [2] G. E. Bergey, R. D. Squires, and W. C. Sipple, "Electrocardiogram recording with pasteless electrodes," *IEEE Trans. Biomed. Eng.*, vol. BME-18, no. 3, pp. 206–2011, May 1971.
- [3] D. E. Hokanson, D. S. Sumner, and D. E. Strandness, "Electrically calibrated plethysmograph for direct measurement of limb blood-flow," *IEEE Trans. Biomed. Eng.*, vol. BME-22, no. 1, pp. 25–29, Jan. 1975.
- [4] M. Garbey, N. Sun, A. Merla, and I. Pavlidis, "Contact-free measurement of cardiac pulse based on the analysis of thermal imagery," *IEEE Trans. Biomed. Eng.*, vol. 54, no. 8, pp. 1418–1426, Aug. 2007.
- [5] M. Z. Poh, D. J. McDuff, and R. W. Picard, "Advancements in non-contact, multiparameter physiological measurements using a webcam," *IEEE Trans. Biomed. Eng.*, vol. 58, no. 1, pp. 7–11, Jan. 2011.
- [6] C. G. Scully, J. Lee, J. Meyer, A. M. Gorbach, D. Granquist-Fraser, Y. Mendelson, and K. H. Chon, "Physiological parameter monitoring from optical recordings with a mobile phone," *IEEE Trans. Biomed. Eng.*, vol. 59, no. 2, pp. 303–306, Feb. 2012.
- [7] O. T. Inan, D. Park, L. Giovannardi, and G. T. A. Kovacs, "Noninvasive measurement of physiological signals on a modified home bathroom scale," *IEEE Trans. Biomed. Eng.*, vol. 59, no. 8, pp. 2137–2143, Aug. 2012.
- [8] M. Mollazadeh, K. Murari, G. Cauwenberghs, and N. V. Thakor, "Wireless micropower instrumentation for multimodal acquisition of electrical and chemical neural activity," *IEEE Trans. Biomed. Circuits Syst.*, vol. 3, no. 6, pp. 388–397, Dec. 2009.
- [9] Y. M. Chi, T.-P. Jung, and G. Cauwenberghs, "Dry-contact and noncontact biopotential electrodes: Methodological review," *IEEE Rev. Biomed. Eng.*, vol. 3, pp. 106–119, Oct. 2010.
- [10] Cognionics Inc., "High density dry EEG headset system spec sheet." [Online]. Available: <http://www.cognionics.com>
- [11] Y. M. Chi, S. R. Deiss, and G. Cauwenberghs, "Non-contact low power EEG/ECG electrode for high density wearable biopotential sensor networks," in *Proc. 6th Int. Workshop Wearable Implantable Body Sens. Netw.*, 2009, pp. 246–250.
- [12] Y. M. Chi, C. Maier, and G. Cauwenberghs, "Ultra-high input impedance, low noise integrated amplifier for noncontact biopotential sensing," *IEEE J. Emerg. Sel. Topics Circuits Syst.*, vol. 1, no. 4, pp. 526–535, Dec. 2011.

- [13] A. Searle and L. Kirkup, "A direct comparison of wet, dry and insulating bioelectric recording electrodes," *Physiol. Meas.*, vol. 21, no. 2, pp. 271–283, 2000.
- [14] A. Baba and M. Burke, "Measurement of the electrical properties of ungelled ECG electrodes," *Int. J. Biol. Biomed. Eng.*, vol. 2, no. 3, pp. 89–97, 2008.
- [15] P. Metherall, D. C. Barber, R. H. Smallwood, and B. H. Brown, "Three-dimensional electrical impedance tomography," *Nature*, vol. 380, no. 6574, pp. 509–512, 1996.
- [16] R. H. Bayford, "Bioimpedance tomography (electrical impedance tomography)," *Annu. Rev. Biomed. Eng.*, vol. 8, pp. 63–91, 2006.
- [17] T. E. Kerner, K. D. Paulsen, A. Hartov, S. K. Soho, and S. P. Poplack, "Electrical impedance spectroscopy of the breast: Clinical imaging results in 26 subjects," *IEEE Trans. Med. Imag.*, vol. 21, no. 6, pp. 638–645, Jun. 2002.
- [18] T. Tidswell, A. Gibson, R. H. Bayford, and D. S. Holder, "Three-dimensional electrical impedance tomography of human brain activity," *Neuroimage*, vol. 13, no. 2, pp. 283–294, 2001.
- [19] A. P. Bagshaw, A. D. Liston, R. H. Bayford, A. Tizzard, A. P. Gibson, A. T. Tidswell, M. K. Sparkes, H. Dehghani, C. D. Binnie, and D. S. Holder, "Electrical impedance tomography of human brain function using reconstruction algorithms based on the finite element method," *Neuroimage*, vol. 20, no. 2, pp. 752–764, 2003.
- [20] R. P. Henderson and J. G. Webster, "An impedance camera for spatially specific measurements of the thorax," *IEEE Trans. Biomed. Eng.*, vol. BME-25, no. 3, pp. 250–254, May 1978.
- [21] I. F. Triantis, A. Demosthenous, M. Rahal, H. Hongwei, and R. Bayford, "A multi-frequency bioimpedance measurement ASIC for electrical impedance tomography," in *Proc. Proc. Eur. Solid-State Circuits Conf.*, 2011, pp. 331–334.
- [22] R. F. Yazicioglu, P. Merken, R. Puers, and C. van Hoof, "A 200 μ W eight-channel EEG acquisition ASIC for ambulatory EEG systems," *IEEE J. Solid-State Circuits*, vol. 43, no. 12, pp. 3025–3038, Dec. 2008.
- [23] N. Van Helleputte, S. Kim, H. Kim, J. P. Kim, C. Van Hoof, and R. F. Yazicioglu, "A 160 μ A biopotential acquisition IC with fully integrated IA and motion artifact suppression," *IEEE Trans. Biomed. Circuits Syst.*, vol. 6, no. 6, pp. 552–561, Dec. 2012.
- [24] S. Kim, R. F. Yazicioglu, T. Torfs, B. Dilpreet, P. Julien, and C. Van Hoof, "A 2.4 μ A continuous-time electrode-skin impedance measurement circuit for motion artifact monitoring in ECG acquisition systems," in *Proc. Symp. VLSI Circuits Digest Techn. Papers*, 2010, pp. 219–220.
- [25] R. Yazicioglu, S. Kim, T. Torfs, H. Kim, and C. Van Hoof, "A 30 μ W analog signal processor ASIC for portable biopotential signal monitoring," *IEEE J. Solid-State Circuits*, vol. 46, no. 1, pp. 209–223, Jan. 2011.
- [26] D. Buxi, S. Kim, N. van Helleputte, M. Altini, J. Wijnsman, R. F. Yazicioglu, J. Penders, and C. van Hoof, "Correlation between electrode-tissue impedance and motion artifact in biopotential recordings," *IEEE Sens. J.*, vol. 12, no. 12, pp. 3373–3383, Dec. 2012.
- [27] B. B. Winter and J. G. Webster, "Reduction of interference due to common-mode voltage in biopotential amplifiers," *IEEE Trans. Biomed. Eng.*, vol. BE-30, no. 1, pp. 58–62, Jan. 1983.
- [28] B. B. Winter and J. G. Webster, "Driven-right-leg circuit-design," *IEEE Trans. Biomed. Eng.*, vol. BME-30, no. 1, pp. 62–66, Jan. 1983.
- [29] S. C. Bunce, M. Izzetoglu, K. Izzetoglu, B. Onaral, and K. Pourrezaei, "Functional near-infrared spectroscopy," *IEEE Eng. Med. Biol. Mag.*, vol. 25, no. 4, pp. 54–62, Jul./Aug. 2006.
- [30] R. Sarpeshkar, *Ultra Low Power Bioelectronics: Fundamentals, Biomedical Applications, and Bio-Inspired Systems*. Cambridge, U.K.: Cambridge Univ. Press, 2010.
- [31] K. Li and S. Warren, "A wireless reflectance pulse oximeter with digital baseline control for unfiltered photoplethysmograms," *IEEE Trans. Biomed. Circuits Syst.*, vol. 6, no. 3, pp. 269–278, Jun. 2012.
- [32] R. G. Haahr, S. B. Duun, M. H. Toft, B. Belhage, J. Larsen, K. Birkelund, and E. V. Thomsen, "An electronic patch for wearable health monitoring by reflectance pulse oximetry," *IEEE Trans. Biomed. Circuits Syst.*, vol. 6, no. 1, pp. 45–53, Feb. 2012.
- [33] E. Kamrani, F. Lesage, and M. Sawan, "Low-noise, high-gain transimpedance amplifier integrated with SiAPD for low-intensity near-infrared light detection," *IEEE Sens. J.*, vol. 14, no. 1, pp. 258–269, Jan. 2014.
- [34] E. Huigen, A. Peper, and C. A. Grimbergen, "Investigation into the origin of the noise of surface electrodes," *Med. Biolog. Eng. Comput.*, vol. 40, no. 3, pp. 332–338, 2002.
- [35] S. Nishimura, Y. Tomita, and T. Horiuchi, "Clinical application of an active electrode using an operational amplifier," *IEEE Trans. Biomed. Eng.*, vol. 39, no. 10, pp. 1096–1099, Oct. 1992.
- [36] M. Fernandez and R. Pallas-Areny, "A simple active electrode for power line interference reduction in high resolution biopotential measurements," in *Proc. 18th Annu. Int. Conf. IEEE Eng. Med. Biol. Soc.*, 1996, vol. 1, pp. 97–98.
- [37] T. Degen and H. Jackel, "Enhancing interference rejection of preamplified electrodes by automated gain adaption," *IEEE Trans. Biomed. Eng.*, vol. 51, no. 11, pp. 2031–2039, Nov. 2004.
- [38] Y. M. Chi and G. Cauwenberghs, "Wireless non-contact eeg/ecg electrodes for body sensor networks," in *Proc. Int. Conf. Body Sens. Netw.*, 2010, pp. 297–301.
- [39] J. Xu, R. F. Yazicioglu, B. Grundlehner, P. Harpe, K. A. A. Makinwa, and C. Van Hoof, "A 160 μ W 8-channel active electrode system for EEG monitoring," *IEEE Trans. Biomed. Circuits Syst.*, vol. 5, no. 6, pp. 555–567, Dec. 2011.
- [40] A. Griffiths, A. Das, B. Fernandes, and P. Gaydecki, "A portable system for acquiring and removing motion artefact from ECG signals," *J. Phys., Conf. Series*, vol. 76, no. 1, p. 012038, 2007.
- [41] S. Kim, H. Kim, N. Van Helleputte, C. Van Hoof, and R. F. Yazicioglu, "Real time digitally assisted analog motion artifact reduction in ambulatory ECG monitoring system," in *Proc. 34th Annu. Int. Conf. IEEE Eng. Med. Biol. Soc.*, 2012, pp. 2096–2099.
- [42] H. Kim, S. Kim, N. Van Helleputte, T. Berset, G. Di, I. Romero, J. Penders, C. Van Hoof, and R. F. Yazicioglu, "Motion artifact removal using cascade adaptive filtering for ambulatory ECG monitoring system," in *Proc. 2012 IEEE Biomed. Circuits Syst. Conf.*, pp. 160–163.
- [43] J. G. Webster, *Medical Instrumentation: Application and Design*, 4th ed. New York, NY, USA: Wiley, 2010.
- [44] R. F. Yazicioglu, C. van Hoof, and R. Puers, *Biopotential Readout Circuits for Portable Acquisition Systems*. New York, NY, USA: Springer-Verlag, 2009.
- [45] S. Kim, L. Yan, S. Mitra, M. Osawa, Y. Harada, K. Tamiya, C. Van Hoof, and R. F. Yazicioglu, "A 20 μ W intra-cardiac signal-processing IC with 82dB bio-impedance measurement dynamic range and analog feature extraction for ventricular fibrillation detection," in *Proc. IEEE Int. Solid-State Circuits Conf. Digest Techn. Papers*, 2013, pp. 302–303.
- [46] K. N. Glaros and E. M. Drakakis, "Trade-offs for low power integrated pulse oximeters," in *Proc. IEEE Biomed. Circuits Syst. Conf.*, 2009, pp. 245–248.
- [47] M. Tavakoli, L. Turicchia, and R. Sarpeshkar, "An ultra-low-power pulse oximeter implemented with an energy-efficient transimpedance amplifier," *IEEE Trans. Biomed. Circuits Syst.*, vol. 4, no. 1, pp. 27–38, Feb. 2010.
- [48] J. K. Choi, M. G. Choi, J. M. Kim, and H. M. Bae, "Efficient data extraction method for near-infrared spectroscopy (NIRS) systems with high spatial and temporal resolution," *IEEE Trans. Biomed. Circuits Syst.*, vol. 7, no. 2, pp. 169–177, Apr. 2013.
- [49] E. Kamrani, F. Lesage, and M. Sawan, "Fully on-chip integrated photodetector front-end dedicated to real-time portable optical brain imaging," *Opt. Photon. J.*, vol. 2, no. 4, pp. 300–313, 2012.
- [50] C. Mead, *Introduction to VLS Systems*. Reading, MA, USA: Addison-Wesley, 1979.
- [51] R. Sarpeshkar, T. Delbruck, and C. A. Mead, "White noise in MOS transistors and resistors," *IEEE Circuits Devices Mag.*, vol. 9, no. 6, pp. 23–29, Nov. 1993.
- [52] A. L. Mcwhorter, "1/f noise and related surface effects in germanium," Ph.D. dissertation, Massachusetts Inst. Technol., Cambridge, MA, USA 1955.
- [53] A. van der Ziel, "Unified presentation of 1/f noise in electron devices: Fundamental 1/f noise sources," *Proc. IEEE*, vol. 76, no. 3, pp. 233–258, May 1988.
- [54] C. C. Enz and G. C. Temes, "Circuit techniques for reducing the effects of op-amp imperfections: Autozeroing, correlated double sampling, and chopper stabilization," *Proc. IEEE*, vol. 84, no. 11, pp. 1584–1614, Nov. 1996.
- [55] M. J. Burke and D. T. Gleeson, "A micropower dry-electrode ECG preamplifier," *IEEE Trans. Biomed. Eng.*, vol. 47, no. 2, pp. 155–162, Feb. 2000.
- [56] R. R. Harrison and C. Charles, "A low-power low-noise CMOS amplifier for neural recording applications," *IEEE J. Solid-State Circuits*, vol. 38, no. 6, pp. 958–965, Jun. 2003.
- [57] M. Mollazadeh, K. Murari, G. Cauwenberghs, and N. Thakor, "Micropower CMOS integrated low-noise amplification, filtering, and digitization of multimodal neuropotentials," *IEEE Trans. Biomed. Circuits Syst.*, vol. 3, no. 1, pp. 1–10, Feb. 2009.
- [58] R. R. Harrison, "The design of integrated circuits to observe brain activity," *Proc. IEEE*, vol. 96, no. 7, pp. 1203–1216, Jul. 2008.

- [59] M. S. J. Steyaert, W. M. C. Sansen, and Z. Y. Chang, "A micropower low-noise monolithic instrumentation amplifier for medical purposes," *IEEE J. Solid-State Circuits*, vol. 22, no. 6, pp. 1163–1168, Dec. 1987.
- [60] K. A. Ng and P. K. Chan, "A CMOS analog front-end IC for portable EEG/ECG monitoring applications," *IEEE Trans. Circuits Syst. I-Regular Papers*, vol. 52, no. 11, pp. 2335–2347, Nov. 2005.
- [61] H. Wu and Y. P. Xu, "A 1V 2.3 μ W biomedical signal acquisition IC," in *Proc. IEEE Int. Solid-State Circuits Conf. Digest Tech. Papers*, 2006, pp. 119–128.
- [62] T. Denison, K. Consoer, W. Santa, A. T. Avestruz, J. Cooley, and A. Kelly, "A 2 μ W 100 nV/rtHz chopper-stabilized instrumentation amplifier for chronic measurement of neural field potentials," *IEEE J. Solid-State Circuits*, vol. 42, no. 12, pp. 2934–2945, Dec. 2007.
- [63] R. F. Yazicioglu, P. Merken, R. Puers, and C. Van Hoof, "A 60 μ W 60 nV/rtHz readout front-end for portable biopotential acquisition systems," *IEEE J. Solid-State Circuits*, vol. 42, no. 5, pp. 1100–1110, May 2007.
- [64] R. Wu, K. A. A. Makinwa, and J. H. Huijsing, "A chopper current-feedback instrumentation amplifier with a 1 mHz 1/ f noise corner and an AC-coupled ripple reduction loop," *IEEE J. Solid-State Circuits*, vol. 44, no. 12, pp. 3232–3243, Dec. 2009.
- [65] X. Zou, X. Xu, L. Yao, and Y. Lian, "A 1-V 450-nW fully integrated programmable biomedical sensor interface chip," *IEEE J. Solid-State Circuits*, vol. 44, no. 4, pp. 1067–1077, Apr. 2009.
- [66] N. Verma, A. Shoeb, J. Bohorquez, J. Dawson, J. Gutttag, and A. P. Chandrakasan, "A micro-power EEG acquisition SoC with integrated feature extraction processor for a chronic seizure detection system," *IEEE J. Solid-State Circuits*, vol. 45, no. 4, pp. 804–816, Apr. 2010.
- [67] Q. W. Fan, F. Sebastiano, J. H. Huijsing, and K. A. A. Makinwa, "A 1.8 μ W 60 nV/rtHz capacitively-coupled chopper instrumentation amplifier in 65 nm CMOS for wireless sensor nodes," *IEEE J. Solid-State Circuits*, vol. 46, no. 7, pp. 1534–1543, Jul. 2011.
- [68] F. Zhang, J. Holleman, and B. P. Otis, "Design of ultra-low power biopotential amplifiers for biosignal acquisition applications," *IEEE Trans. Biomed. Circuits Syst.*, vol. 6, no. 4, pp. 344–355, Aug. 2012.
- [69] Y. Tseng, Y. C. Ho, S. T. Kao, and C. C. Su, "A 0.09 μ W low power front-end biopotential amplifier for biosignal recording," *IEEE Trans. Biomed. Circuits Syst.*, vol. 6, no. 5, pp. 508–516, Oct. 2012.
- [70] J. Yoo, L. Yan, D. El-Damak, M. A. Bin Altaf, A. H. Shoeb, and A. P. Chandrakasan, "An 8-channel scalable EEG acquisition SoC with patient-specific seizure classification and recording processor," *IEEE J. Solid-State Circuits*, vol. 48, no. 1, pp. 214–228, Jan. 2013.
- [71] R. Muller, S. Gambini, and J. M. Rabaey, "A 0.013mm² 5 μ W DC-coupled neural signal acquisition IC with 0.5V supply," in *Proc. IEEE Int. Solid-State Circuits Conf. Digest Techn. Papers*, 2011, pp. 302–304.
- [72] D. Han, Y. Zheng, R. Rajkumar, G. Dawe, and M. Je, "A 0.45V 100-channel neural-recording IC with sub- μ W/channel consumption in 0.18 μ m CMOS," in *Proc. IEEE Int. Solid-State Circuits Conf. Dig. Techn. Papers*, 2013, pp. 290–291.
- [73] T. Delbruck and C. A. Mead, "Adaptive photoreceptor with wide dynamic range," in *Proc. IEEE Int. Symp. Circuits Syst.*, 1994, vol. 4, pp. 339–342.
- [74] J. L. Bohorquez, M. Yip, A. P. Chandrakasan, and J. L. Dawson, "A biomedical sensor interface with a sinc filter and interference cancellation," *IEEE J. Solid-State Circuits*, vol. 46, no. 4, pp. 746–756, Apr. 2011.
- [75] F. Zhang, A. Mishra, A. G. Richardson, and B. Otis, "A low-power ECoG/EEG processing IC with integrated multiband energy extractor," *IEEE Trans. Circuits Syst. I, Reg. Papers*, vol. 58, no. 9, pp. 2069–2082, Sep. 2011.
- [76] W. Wattanapanitch, M. Fee, and R. Sarpeshkar, "An energy-efficient micropower neural recording amplifier," *IEEE Trans. Biomed. Circuits Syst.*, vol. 1, no. 2, pp. 136–147, Jun. 2007.
- [77] R. H. Olsson, D. L. Buhl, A. M. Sirota, G. Buzsaki, and K. D. Wise, "Band-tunable and multiplexed integrated circuits for simultaneous recording and stimulation with microelectrode arrays," *IEEE Trans. Biomed. Eng.*, vol. 52, no. 7, pp. 1303–1311, Jul. 2005.
- [78] M. S. Chae, Z. Yang, M. R. Yuze, L. Hoang, and W. T. Liu, "A 128-channel 6 mW wireless neural recording IC with spike feature extraction and UWB transmitter," *IEEE Trans. Neural Syst. Rehabil. Eng.*, vol. 17, no. 4, pp. 312–321, Aug. 2009.
- [79] M. T. Shiu, K. W. Yao, and C. S. A. Gong, "Tunable high resistance voltage-controlled pseudo-resistor with wide input voltage swing capability," *Electron. Lett.*, vol. 47, no. 6, pp. 377–378, 2011.
- [80] H. Nyquist, "Thermal agitation of electric charge in conductors," *Phys. Rev.*, vol. 32, no. 1, pp. 110–113, 1928.
- [81] J. B. Johnson, "Thermal agitation of electricity in conductors," *Phys. Rev.*, vol. 32, no. 1, pp. 97–109, 1928.
- [82] Y. Chen, A. Basu, and M. Je, "A digitally assisted, pseudo-resistor-less amplifier in 65nm CMOS for neural recording applications," in *Proc. IEEE 55th Int. Midwest Symp. Circuits Syst.*, 2012, pp. 366–369.
- [83] K. C. Hsieh, P. R. Gray, D. Senderowicz, and D. G. Messerschmitt, "A low-noise chopper-stabilized differential switched-capacitor filtering technique," *IEEE J. Solid-State Circuits*, vol. 16, no. 6, pp. 708–715, Dec. 1981.
- [84] C. C. Enz, E. A. Vittoz, and F. Krummenacher, "A CMOS chopper amplifier," *IEEE J. Solid-State Circuits*, vol. 22, no. 3, pp. 335–342, Jun. 1987.
- [85] C. Menolfi and Q. T. Huang, "A low-noise CMOS instrumentation amplifier for thermoelectric infrared detectors," *IEEE J. Solid-State Circuits*, vol. 32, no. 7, pp. 968–976, Jul. 1997.
- [86] C. Menolfi and Q. T. Huang, "A fully integrated, untrimmed CMOS instrumentation amplifier with submicrovolt offset," *IEEE J. Solid-State Circuits*, vol. 34, no. 3, pp. 415–420, May 1999.
- [87] R. Burt and J. Zhang, "A micropower chopper-stabilized operational amplifier using a SC notch filter with synchronous integration inside the continuous-time signal path," *IEEE J. Solid-State Circuits*, vol. 41, no. 12, pp. 2729–2736, Dec. 2006.
- [88] L. Fay, V. Misra, and R. Sarpeshkar, "A micropower electrocardiogram amplifier," *IEEE Trans. Biomed. Circuits Syst.*, vol. 3, no. 5, pp. 312–320, Oct. 2009.
- [89] M. A. Haberman and E. M. Spinelli, "A multichannel EEG acquisition scheme based on single ended amplifiers and digital DRL," *IEEE Trans. Biomed. Circuits Syst.*, vol. 6, no. 6, pp. 614–618, Dec. 2012.
- [90] L. Yan, J. Bae, S. Lee, B. Kim, T. Roh, K. Song, and H.-J. Yoo, "A 3.9mW 25-electrode reconfigured thoracic impedance/ECG SoC with body-channel transponder," in *Proc. IEEE Int. Solid-State Circuits Conf. Digest Tech. Papers*, 2010, pp. 490–491.
- [91] N. Verma and A. P. Chandrakasan, "An ultra low energy 12-bit rate-resolution scalable SAR ADC for wireless sensor nodes," *IEEE J. Solid-State Circuits*, vol. 42, no. 6, pp. 1196–1205, Jun. 2007.
- [92] L. Yan, J. Yoo, B. Kim, and H. J. Yoo, "A 0.5- μ V_{rms} 12- μ W wirelessly powered patch-type healthcare sensor for wearable body sensor network," *IEEE J. Solid-State Circuits*, vol. 45, no. 11, pp. 2356–2365, Nov. 2010.
- [93] S. Lee, L. Yan, T. Roh, S. Hong, and H. J. Yoo, "A 75 μ W real-time scalable body area network controller and a 25 μ W ExG sensor IC for compact sleep monitoring applications," *IEEE J. Solid-State Circuits*, vol. 47, no. 1, pp. 323–334, Jan. 2012.
- [94] M. Khayatizadeh, X. Zhang, J. Tan, W. S. Liew, and Y. Lian, "A 0.7-V 17.4- μ W 3-lead wireless ECG SoC," *IEEE Trans. Biomed. Circuits Syst.*, vol. 7, no. 5, pp. 583–592, Oct. 2013.
- [95] Y.-J. Min, H.-K. Kim, Y.-R. Kang, G.-S. Kim, J. Park, and S.-W. Kim, "Design of wavelet-based ECG detector for implantable cardiac pacemakers," *IEEE Trans. Biomed. Circuits Syst.*, vol. 7, no. 4, pp. 426–436, Aug. 2013.
- [96] J. L. McCreary and P. R. Gray, "All-MOS charge redistribution analog-to-digital conversion techniques-Part I," *IEEE J. Solid-State Circuits*, vol. SSC-10, no. 6, pp. 371–379, Dec. 1975.
- [97] R. E. Suarez, P. R. Gray, and D. A. Hodges, "All-MOS charge redistribution analog-to-digital conversion techniques-Part II," *IEEE J. Solid-State Circuits*, vol. SSC-10, no. 6, pp. 379–385, Dec. 1975.
- [98] A. Agnes, E. Bonizzoni, P. Malcovati, and F. Maloberti, "A 9.4-ENOB 1V 3.8 μ W 100k/s SAR ADC with time-domain comparator," in *Proc. IEEE Int. Solid-State Circuits Conf. Digest Techn. Papers*, 2008, pp. 246–610.
- [99] B. P. Ginsburg and A. P. Chandrakasan, "An energy-efficient charge recycling approach for a SAR converter with capacitive DAC," in *Proc. IEEE Int. Symp. Circuits Syst.*, 2005, pp. 184–187.
- [100] Y. M. Chi and G. Cauwenberghs, "Micropower integrated bioamplifier and auto-ranging ADC for wireless and implantable medical instrumentation," in *Proc. Eur. Solid-State Circuits Conf.*, 2010, pp. 334–337.
- [101] S. Ha, J. Park, Y. M. Chi, J. Viventi, J. Rogers, and G. Cauwenberghs, "85 dB dynamic range 1.2 mW 156 kS/s biopotential recording IC for high-density ECoG flexible active electrode array," in *Proc. Eur. Solid-State Circuits Conf.*, 2013, pp. 141–144.

- [102] J. Garcia, S. Rodriguez, and A. Rusu, "A low-power CT incremental 3rd order sigma delta ADC for biosensor applications," *IEEE Trans. Circuits Syst. I, Reg. Papers*, vol. 60, no. 1, pp. 25–36, Jan. 2013.
- [103] J. R. Custodio, J. Goes, N. Paulino, J. P. Oliveira, and E. Bruun, "A 1.2-V 165- μ W 0.29-mm² multibit sigma-delta ADC for hearing aids using nonlinear DACs and with over 91 dB dynamic-range," *IEEE Trans. Biomed. Circuits Syst.*, vol. 7, no. 3, pp. 376–385, Jun. 2013.
- [104] L. Yongjia, Z. Duan, and W. A. Serdijn, "A sub-microwatt asynchronous level-crossing ADC for biomedical applications," *IEEE Trans. Biomed. Circuits Syst.*, vol. 7, no. 2, pp. 149–157, Apr. 2013.
- [105] W. Tang, A. Osman, D. Kim, B. Goldstein, C. X. Huang, B. Martini, V. A. Pieribone, and E. Culurciello, "Continuous time level crossing sampling ADC for bio-potential recording systems," *IEEE Trans. Circuits Syst. I, Reg. Papers*, vol. 60, no. 6, pp. 1407–1418, Jun. 2013.
- [106] H. Y. Yang and R. Sarpeshkar, "A bio-inspired ultra-energy-efficient analog-to-digital converter for biomedical applications," *IEEE Trans. Circuits Syst. I, Reg. Papers*, vol. 53, no. 11, pp. 2349–2356, Nov. 2006.
- [107] B. Murmann, "ADC performance survey 1997-2013." [Online]. Available: <http://www.stanford.edu/~murmman/adcsurvey.html>
- [108] H. C. Hong and G. M. Lee, "A 65-fJ/conversion-step 0.9-V 200-kS/s rail-to-rail 8-bit successive approximation ADC," *IEEE J. Solid-State Circuits*, vol. 42, no. 10, pp. 2161–2168, Oct. 2007.
- [109] J. Sauerbrey, D. Schmitt-Landsiedel, and R. Thewes, "A 0.5-V 1- μ W successive approximation ADC," *IEEE J. Solid-State Circuits*, vol. 38, no. 7, pp. 1261–1265, Jul. 2003.
- [110] M. Yip and A. P. Chandrakasan, "A resolution-reconfigurable 5-to-10b 0.4-to-1V power scalable SAR ADC," in *Proc. IEEE Int. Solid-State Circuits Conf. Digest Tech. Papers*, 2011, pp. 190–192.
- [111] A. Ueno and Y. Yama, "Unconstrained monitoring of ECG and respiratory variation in infants with underwear during sleep using a bed-sheet electrode unit," in *Proc. 30th Annu. Int. Conf. IEEE Eng. Med. Biol. Soc.*, 2008, pp. 2329–2332.
- [112] A. Ueno, Y. Akabane, T. Kato, H. Hoshino, S. Kataoka, and Y. Ishiyama, "Capacitive sensing of electrocardiographic potential through cloth from the dorsal surface of the body in a supine position: A preliminary study," *IEEE Trans. Biomed. Eng.*, vol. 54, no. 4, pp. 759–766, Apr. 2007.
- [113] Y. G. Lim, K. K. Kim, and K.-S. Park, "ECG recording on a bed during sleep without direct skin-contact," *IEEE Trans. Biomed. Eng.*, vol. 54, no. 4, pp. 718–725, Apr. 2007.
- [114] A. Ueno, Y. Shiogai, and Y. Ishiyama, "A primary study of indirect ECG monitor embedded in a bed for home health care," *IEEE Trans. Electron., Inf. Syst.*, vol. 127, no. 10, pp. 1792–1799, 2007.
- [115] A. Ueno, T. Imai, D. Kowada, and Y. Yama, *Capacitive Sensing of Narrow-Band ECG and Breathing Activity of Infants Through Sleepwear*. Vukovar, Croatia: InTech, 2009, ch. 21, pp. 399–414.
- [116] Y. Yama and A. Ueno, "Unrestrained facile measurement of narrow-band ECG and respiratory variation in infants with a capacitive sheet-type sensor," *Trans. Japanese Soc. Med. Biolog. Eng.*, vol. 47, no. 1, pp. 42–50, 2009.
- [117] M. Ohtsu, Y. Fukuoka, and A. Ueno, "Underwater electromyographic measurement using a water-proof insulated electrode," *Adv. Biomed. Eng.*, vol. 1, pp. 81–88, 2012.
- [118] Cognionics Inc., "Dry ECG belt spec sheet." [Online]. Available: <http://www.cognionics.com>



Sohyung Ha (S'05) received the B.S. degree (with *summa cum laude*) and the M.S. degree in electrical engineering from the Korea Advanced Institute of Science and Technology, Daejeon, Korea, in 2004 and 2006, respectively. He is currently working toward the Ph.D. degree from the Department of Bioengineering, University of California San Diego, La Jolla, CA, USA.

From 2006 to 2010, he was with Samsung Electronics as an Analog and Mixed-Signal Circuit Designer for commercial multimedia devices. His research interests include integrated circuits and interfaces for implantable and wearable biosignal monitoring and actuation systems. He received the Fulbright Fellowship from 2010 to 2012.



Chul Kim (S'13) received the B.S. degree from the Kyungpook National University, Daegu, Korea, in 2007, and the M.S. degree from the Korea Advanced Institute of Science and Technology, Daejeon, Korea, in 2009, both in electrical engineering. He is currently working toward the Ph.D. degree from the Department of Bioengineering, The University of California, San Diego, CA, USA.

He was with SK HYNIX, Gyeonggi, Korea, as a Power Circuitry Designer for DRAM from 2009 to 2012. His research interests include designing analog integrated circuits and power management ICs for biomedical applications.



Yu M. Chi (S'04–M'11) received the B.S. degree in electrical engineering from the Johns Hopkins University, Baltimore, MD, USA, in 2007, and the Ph.D. degree in electrical engineering from the University of California San Diego, La Jolla, CA, USA, in 2011.

He is currently the Chief Technology Officer at Cognionics, Inc., San Diego, CA, USA, working on wireless and noncontact biopotential sensing systems.



Abraham Akinin (S'13) was born in Caracas, Venezuela. He received the B.S. degree in biomedical engineering and physics from the University of Miami, Coral Gables, FL, USA, in 2010. He is currently working toward the Ph.D. degree from Department of Bioengineering, the University of California San Diego, La Jolla, CA, USA, and the Institute for Neural Computation, La Jolla.

His research interests include closed-loop medical instrumentation and neuroprosthetics.



Christoph Maier (S'97–M'00) received the Diplom-Physiker degree from the University of Heidelberg, Heidelberg, Germany, in 1995, and the Dr.sc. degree in electrical engineering from the Swiss Federal Institute of Technology Zurich, Switzerland, in 2000.

After time in industry, he joined the Integrated Systems Neuroengineering laboratory at the University of California San Diego, La Jolla, CA, USA, as Postdoctoral Researcher in 2010. His main research interests include interfaces for electrophysiological

signals and modeling neural networks in analog VLSI.



Akinori Ueno (M'03) received the Ph.D. degree in biomedical engineering from Keio University, Yokohama, Japan, in 1999.

He is a Professor of electrical and electronic engineering at Tokyo Denki University, Tokyo, Japan, and held a position as an Associate Professor of electrical and computer engineering at Tokyo Denki University, Saitama, Japan. He was a Visiting Scholar at the Department of Bioengineering, University of California-San Diego, La Jolla, CA, USA, from April 2013 to March 2014. His research interests include

biomedical instrumentation and intelligent human-machine interfaces.

Dr. Ueno received several research awards from the Japan Society of Medical Electronics and Biological Engineering, the Society of Life Support Engineering, and the Society of Instrument and Control Engineers.



Gert Cauwenberghs (S'89–M'94–SM'04–F'11) received the M.Eng. degree in applied physics from the University of Brussels, Brussels, Belgium, in 1988, and the M.S. and Ph.D. degrees in electrical engineering from the California Institute of Technology, Pasadena, CA, USA, in 1989 and 1994, respectively.

He is currently a Professor of bioengineering at the University of California, San Diego, CA, where he codirects the Institute for Neural Computation, participates as a member of the Institute of Engineering in Medicine, and serves on the Computational Neuro-

science Executive Committee, Department of Neurosciences graduate program. Previously, he was a Professor of electrical and computer engineering at Johns Hopkins University, Baltimore, MD, USA, and a Visiting Professor of brain and cognitive science at the Massachusetts Institute of Technology, Cambridge, MA, USA. He cofounded and chairs the Scientific Advisory Board of Cognionics Inc. His research interest includes micropower biomedical instrumentation, neuron-silicon, and brain-machine interfaces, neuromorphic engineering, and adaptive intelligent systems.

Dr. Cauwenberghs received the National Science Foundation Career Award in 1997, the ONR Young Investigator Award in 1999, and the Presidential Early Career Award for Scientists and Engineers in 2000. He was Francqui Fellow of the Belgian American Educational Foundation. He was a Distinguished Lecturer of the IEEE Circuits and Systems Society from 2002 to 2003. He continues to serve IEEE in a variety of roles, most recently Cochairing the IEEE Biomedical Circuits and Systems Conference (BioCAS'2011) and the technical program committee of the IEEE Engineering in Medicine and Biology Conference (EMBC'2012), both held in San Diego. He is a Senior Editor for the IEEE SENSORS JOURNAL and the IEEE JOURNAL ON EMERGING AND SELECTED TOPICS IN CIRCUITS AND SYSTEMS, and Editor-in-Chief of the IEEE TRANSACTIONS ON BIOMEDICAL CIRCUITS AND SYSTEMS.